Supplementary Information for

Room-Temperature and Atmospheric-Pressure Direct Wafer Bonding without Stringent Pretreatments Using Ultrafast Lasers

Taoyuan Zhu[1], Zhenyu Hu[1], Qiaohui Yang[2], Yuqiang Yu[1], Ruixue Ding[1], Weilong Wu[1], Bingjie Wang[1], Duo Pan[2], Jingbiao Chen[2], Zhiwei Li[1,*], Xianlong Wei[1,*]

[1]*Key Laboratory for the Physics and Chemistry of Nanodevices, School of Electronics, Peking University, Beijing, China*

[2]*National Key Laboratory of Advanced Micro and Nano Manufacture Technology, School of Electronics, Peking University, Beijing, China.*

* *Corresponding authors. Email: weixl@pku.edu.cn, lzw111@pku.edu.cn*

Supplementary Note 1. Estimation of the air gap thickness

Fig. S1a shows the photograph of the wafers in their natural stacked state before bonding, and the corresponding interference fringe pattern captured by the CMOS camera is shown in Fig. S1b. In both figures, the region highlighted with orange lines corresponds to the location where the interference fringes are densest, indicating the maximum air gap at this site. Based on this observation, we selected this region to estimate the maximum thickness of tolerable gap of ultrafast laser bonding (ULB) employing front-expanding strategy. Statistical analysis reveals that 12 bright fringes are observed in this region. According to the condition for bright fringes in equal-thickness interference:

$$2e + \frac{\lambda_O}{2} = k\lambda_O, k = 1,2,3 \ldots (\text{Bright}) \quad \text{(S1)}$$

where the wavelength of the coaxial light source λ_O = 520 nm, the observed bright fringe order k = 12. Substituting these values yields an estimated gap of 2.99 μm at this location.

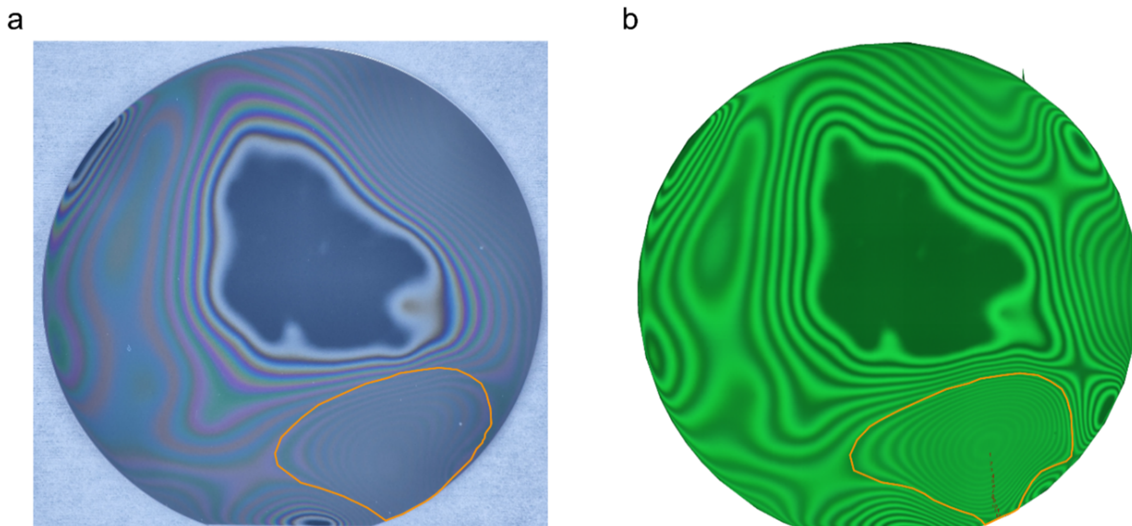

Fig. S1 Estimation of the air gap thickness. a Photograph of wafers in a naturally stacked state before bonding. **b** Interference fringe pattern captured by the CMOS camera. The region enclosed by the orange line indicates the area with the densest interference fringes, and the red numbers label the orders of the bright fringes.

20 ## Supplementary Note 2. Raman spectroscopic analysis

21 We performed a Raman line scan across the interface of the bonded BF33–silicon pair, with a step
22 size of 0.5 μm, to obtain the spatial variation of Raman intensities. The corresponding heat map is shown
23 in Fig. S2a. Typical Raman spectra of monocrystalline silicon, the bonding layer, and glass are presented
24 in Fig. S2b: monocrystalline silicon exhibits a sharp characteristic peak at 520 cm^{-1}; pure glass shows
25 a series of broad peaks in the 400–500 cm^{-1} range; the spectrum of the bonding layer displays an
26 intermediate profile between the two. To determine whether new Si–O–Si bonds were formed in the
27 bonding layer, we integrated the Raman intensities at each position within the wavenumber windows
28 of 445 ± 5 cm^{-1} and 482 ± 5 cm^{-1}, and plotted the results in Fig. 3d of the main text.

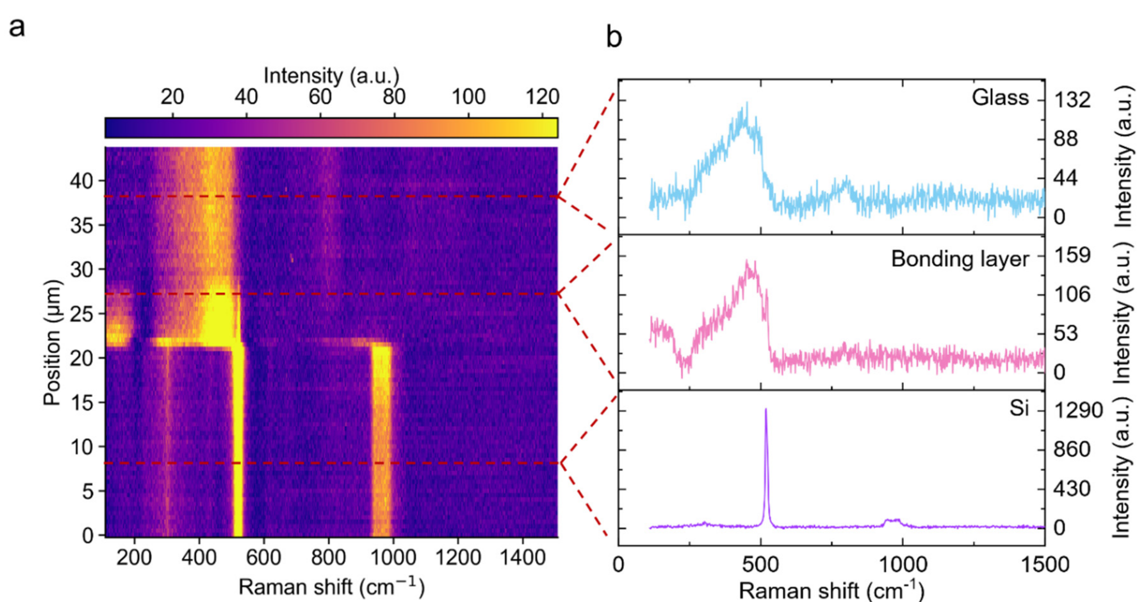

Fig. S2 Raman line scan across the bonding interface. a Heat map showing the spatial distribution of Raman intensities across the entire bonding interface. **b** Typical Raman spectra of monocrystalline silicon, the bonding layer, and glass, with their corresponding positions in **a** indicated by red dashed lines.

29 ## Supplementary Note 3. Wafer-scale fabrication of MEMS atomic vapor cells

30 The MEMS atomic vapor cells adopt a glass–silicon–glass sandwich structure (Fig. 4b in the main
31 text). Two through-holes are fabricated in the silicon layer: a 6.8 mm × 6.8 mm square hole serving as
32 the optical cavity, and a circular hole with a diameter of 1 mm for accommodating the rubidium
33 dispenser. The fabrication process of the wafer-scale MEMS atomic vapor cell is illustrated in Fig. S3.
34 First, through-holes are machined in a 3-mm-thick silicon wafer via sandblasting. Subsequently, the
35 first glass wafer is bonded to the silicon wafer using ULB to form a half-cavity structure. A rubidium
36 dispenser (SAES Getters RB/AMAX/PILL/1-0.6) is then loaded into the small circular hole. Finally,
37 the assembled half-cavity is transferred to a vacuum environment of 10^{-3} Pa, and the second glass wafer
38 is bonded using ultrafast laser to achieve hermetic vacuum sealing. Wafer dicing and activation of the
39 rubidium dispenser are performed subsequently according to testing requirements.

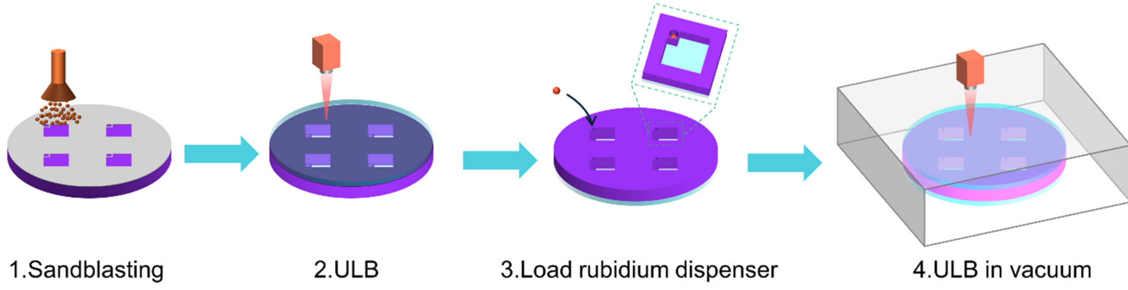

Fig. S3 Fabrication process schematic for wafer-scale MEMS atomic vapor cells.

40 ## Supplementary Note 4. Leak rate estimation of MEMS vapor cells

41 The saturated absorption spectra (SAS) and modulation transfer spectra (MTS) of the MEMS
42 atomic vapor cell measured on Day 0 and Day 21 are shown in Fig. S4a and S4b, respectively. The
43 saturated absorption linewidths of the ^{87}Rb D_2 are 26.62 MHz on Day 0 and 39.20 MHz on Day 21. For
44 the rubidium D2 transition, the total linewidth in SAS is typically expressed as[1]:

49 $$\Gamma_{\mathrm{tot}} = \Gamma_{\mathrm{natural}} + \Gamma_{\mathrm{power}} + \Gamma_{\mathrm{transit}} + \Gamma_{\mathrm{pressure}} \quad (S2)$$

45 where $\Gamma_{\mathrm{natural}}$ is the natural linewidth, Γ_{power} is the power broadening, $\Gamma_{\mathrm{transit}}$ is the transit-time broadening
46 and $\Gamma_{\mathrm{pressure}}$ represents collisional (pressure) broadening. Since all measurements were performed under
47 the same conditions on the same test system, the first three contributions to the linewidth are considered
48 constant, yielding a pressure broadening change of 12.58 MPa.

50 The pressure-induced broadening $\Gamma_{\mathrm{pressure}}$ can be described as[2]:

56 $$\Gamma_{\mathrm{pressure}} = \alpha\rho(T/T_0)^n + \beta \quad (S3)$$

51 where α = 18.83 GHz/amg, ρ is the gas density, $T \approx 333$ K is the vapor cell's operating temperature, T_0
52 = 353 K, n = -0.19. Substituting into Eq. S3 gives the gas density change:

57 $$\Delta\rho = \rho^{Day21} - \rho^{Day0} \approx 6.6 \times 10^{-4}\ \mathrm{amg} \quad (S4)$$

53 Assuming ideal gas behavior, the change in vacuum level inside the cell is:

58 $$\Delta P = \Delta\rho k_B T \approx 81.6\mathrm{Pa} \quad (S5)$$

54 With a cell volume of V = 6.8 mm × 6.8 mm × 3 mm, and a measurement duration of t = 21 days, the
55 leak rate is estimated as:

59 $$Q = \frac{\Delta PV}{t} \approx 6 \times 10^{-12}\mathrm{Pa{\cdot}m^3/s} \quad (S6)$$

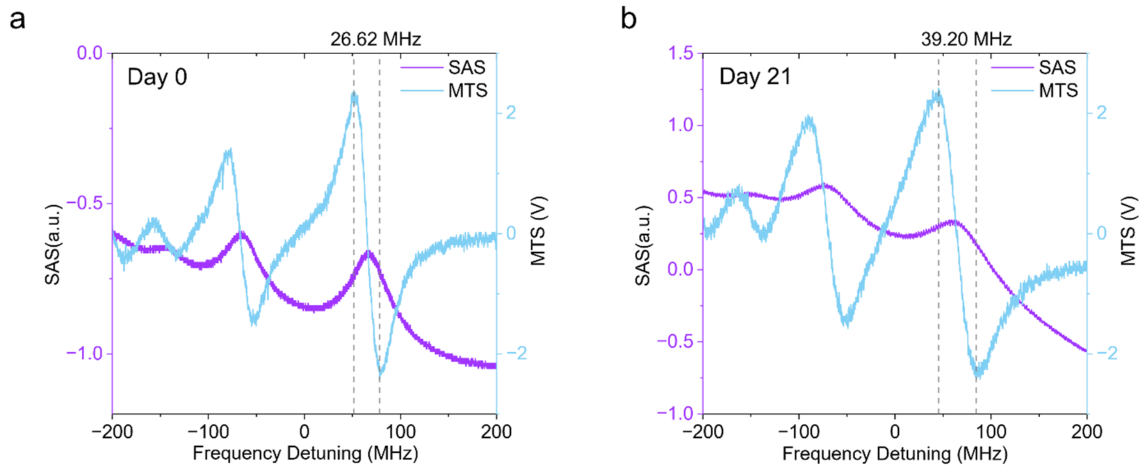

Fig. S4 The performance of the MEMS atomic vapor cell. a SAS and MTS measured on Day 0. **b** SAS and MTS measured on Day 21.

60 **Supplementary Note 5. Interference fringe processing**

61 In this study, machine vision algorithms were employed to process the acquired interference fringe
62 images and to obtain the boundary coordinates of the quasi-optical contact region. Figure S5a shows
63 the original interference fringe image captured by the CMOS camera. Given that the coaxial light source
64 emits green light, we extracted the green channel of the image for processing, and the corresponding
65 grayscale image is presented in Fig. S5b. Theoretically, bright fringes and dark fringes correspond to
66 the maximum and minimum values in the green channel, respectively, so the image was binarized (Fig.
67 S5c). The selection of the binarization threshold in this step is critical, as it directly affects the
68 subsequent fringe recognition. In general, the adaptive threshold algorithm in OpenCV can be used; if
69 the recognition performance is unsatisfactory, manual adjustment of the threshold is required.
70 Subsequently, contour detection was performed on the binarized image, and the orange lines in Fig. S5d
71 represent all detected contours. Finally, after acquiring the positional information of all contours, the
72 hierarchical relationships among these contours were reconstructed. The contour at the desired order
73 was then selected as the boundary of the quasi-optical contact region according to the quasi-optical
74 contact criteria (Fig. S5e).

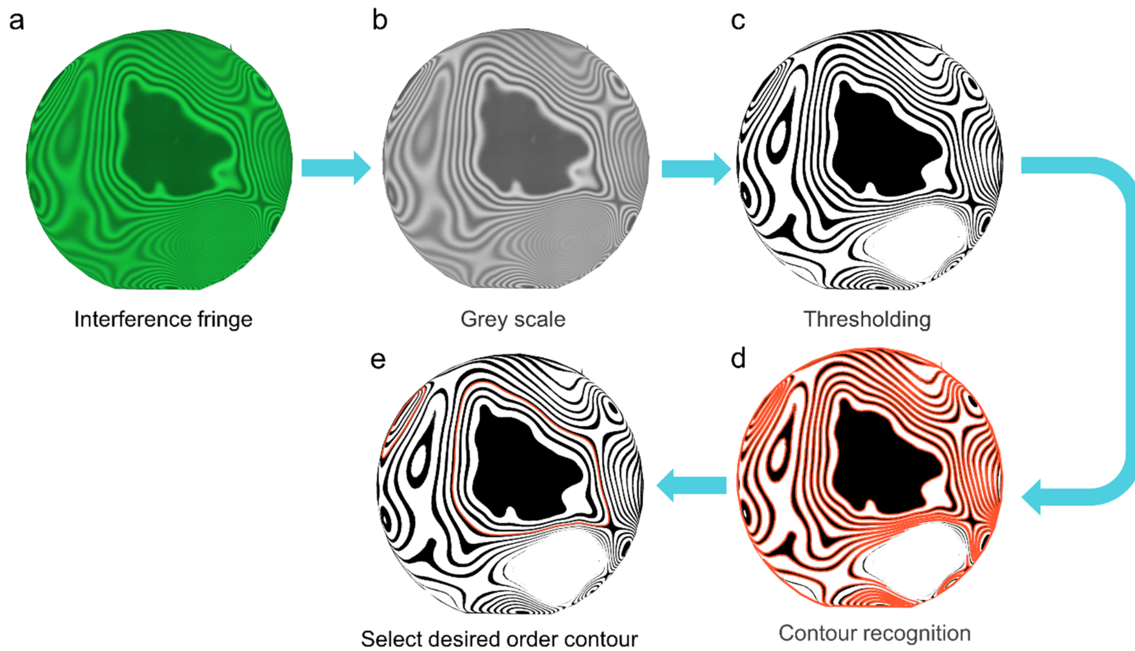

Fig. S5 Machine vision algorithm for interference fringe processing. a Original interference fringe image captured by the CMOS camera. **b** Grayscale image converted from the green channel. **c** Binarized image after threshold processing. **d** Detected contours (orange lines) with hierarchical structure. **e** The desired order contour selected according to the quasi-optical contact criteria.

Supplementary Note 6. Specifications of wafer samples

Table S1. The specifications of wafer samples used in experiments.

Material	Size	Thickness	Polish	Crystal orientation
Si	6-inch wafer	400 μm	double-side	<100>
Si	4-inch wafer	500 μm	double-side	<100>
BF33	6-inch wafer	500 μm	double-side	-
BF33	4-inch wafer	500 μm	double-side	-
Quartz	10 mm × 10 mm	500 μm	double-side	-
Sapphire	10 mm × 10 mm	430 μm	double-side	C-plane
$LiNbO_3$	10 mm × 10 mm	500 μm	double-side	Y-cut
4H-SiC	10 mm × 10 mm	500 μm	double-side	<0001>

References

1. Letokhov, V. S. Saturation spectroscopy. in *High-resolution laser spectroscopy* (ed. Shimoda, K.) 95–171 (Springer, Berlin, Heidelberg, 1976). doi:10.1007/3540077197_20.

2. Kluttz, K. A., Averett, T. D. & Wolin, B. A. Pressure broadening and frequency shift of the D 1 and D 2 lines of Rb and K in the presence of 3 He and N 2. *Phys. Rev. A* **87**, 032516 (2013).